

# Implementation of Radiation, Ablation, and Free Energy Minimization Modules for Coupled Simulations of Hypersonic Flow

Peter A Gnoffo\*

Christopher O Johnston†

Richard A. Thompson‡

*NASA Langley Research Center, Hampton, VA 23681-2199*

A description of models and boundary conditions required for coupling radiation and ablation physics to a hypersonic flow simulation is provided. Chemical equilibrium routines for varying elemental mass fraction are required in the flow solver to integrate with the equilibrium chemistry assumption employed in the ablation models. The capability also enables an equilibrium catalytic wall boundary condition in the non-ablating case. The paper focuses on numerical implementation issues using FIRE II, Mars return, and Apollo 4 applications to provide context for discussion. Variable relaxation factors applied to the Jacobian elements of partial equilibrium relations required for convergence are defined. Challenges of strong radiation coupling in a shock capturing algorithm are addressed. Results are presented to show how the current suite of models responds to a wide variety of conditions involving coupled radiation and ablation.

## I. Nomenclature

Bold face, lowercase variable names refer to vectors. Bold face, uppercase variable names refer to matrices. Bracketed entry indicates units or quantity used to non-dimensionalize.

### Roman symbols

$A_j - E_j$	curve fit constants for $K_j(T)$ to define equilibrium relation for non-base species $j$
$\tilde{c}_{i,abl}$	elemental mass fraction of element $i$ in ablation products
$D_j$	effective diffusion coefficient for species $j$ , [ $L_{ref}V_\infty$ ]
$\mathbf{f}$	species flux vector
$f_{rad}$	fraction of divergence of radiative flux introduced into flow solver (Eq 19)
$\mathbf{F}$	transformation matrix from species continuity to elemental continuity equations
$F_{i,j}$	element of $\mathbf{F}$ defined in Eq. 1
$\Delta F_j^0$	change in free energy in Eqs. 7 and 8, [J/kmole]
$G_{j,k}$	coefficient of $\ln \rho_k$ in partial equilibrium relation for non-base species $j$ (Eq. 10)
$H_n$	enthalpy of species $n$ , [J/kmole]
$K_j(T)$	equilibrium constant for reaction $j$ , Eq. 11
$L_{ref}$	reference length used to non-dimensionalize distance [m]
$\dot{m}$	blowing rate of ablation products per unit area, [ $\rho_\infty V_\infty$ ]

---

\*Senior Research Engineer, Aerothermodynamics Branch; AIAA Fellow

†Research Engineer, Aerothermodynamics Branch; AIAA Member

‡Research Engineer, Aerothermodynamics Branch; AIAA Senior Member

$\tilde{M}_i$	molecular weight of element $i$ , [kg/kmole]
$M_j$	molecular weight of species $j$ , [kg/kmole]
$N_{exchange}$	frequency for updating ghost cells
$N_{rad}$	frequency for updating divergence of radiative flux in interior
$\bar{p}_n$	partial pressure of species $n$ , [atm]
$p$	pressure, $[\rho_\infty V_\infty^2]$
$\mathbf{q}$	vector of dependent variables, species densities $[\rho_\infty]$
$q$	heating rate, [W/m <sup>2</sup> ]
$R$	universal gas constant, 8314.3 [J/K -kmole]
$\bar{R}$	modified gas constant defined below Eq. 9
$S_n$	entropy of species $n$ , [J/kmole-K]
$t$	time $[L_{ref}/V_\infty]$
$T$	temperature [K]
$\dot{\mathbf{w}}$	vector of chemical source terms, $[\rho_\infty V_\infty/L_{ref}]$
$x, y$	distance, Cartesian coordinates $[L_{ref}]$
$u, v$	velocities in $x$ and $y$ directions, respectively, $[V_\infty]$
$\tilde{V}_i$	diffusion velocity of element $i$ , $[V_\infty]$
$V_j$	diffusion velocity of species $j$ , $[V_\infty]$
$V_\infty$	reference velocity in free stream [m/s]
$Z$	10000./T used in Eq. 11

### Greek symbols

$\alpha_{i,j}$	number of atoms of element $i$ in species $j$
$\beta_{m,j}$	stoichiometric coefficient of reactant $m$ in non-base species relation $j$
$\beta_{n,j}$	stoichiometric coefficient of product $n$ in non-base species relation $j$
$\epsilon$	surface emissivity
$\varepsilon$	damping coefficient on surface temperature updates
$\tilde{\rho}_i$	density of element $i$ , $[\rho_\infty]$
$\rho_j$	density of species $j$ , $[\rho_\infty]$
$\rho_\infty$	reference density in free stream, [kg/m <sup>3</sup> ]
$\sigma$	Stefan-Boltzmann constant, $5.66961 \cdot 10^{-8}$ W/(m <sup>2</sup> -K <sup>4</sup> )
$\chi_j$	mole fraction of species $j$

### Subscripts

0	ghost cell behind boundary
1	internal cell adjacent to boundary
$i$	element index
$j$	species index
$k$	species index
$m$	reactant species index
$n$	product species index
$\infty$	reference condition in free stream

## II. Introduction

The design of many planetary entry vehicles requires definition of the aerothermal environment including shock-layer radiation and ablation. In air, shock-layer radiation becomes significant at velocities above 10 km/s for vehicles of order 1 meter diameter or greater. Radiative heating is proportional to the shock-layer

thickness (to some positive fractional power less than or equal to 1 depending on optical thickness of the gas), which increases as the vehicle diameter increases. The radiation (photon transport) cools the shock layer but also directs energy toward the vehicle surface to increase the heating rate. In environments where radiative heating is significant, an ablating thermal protection system is usually required to protect the vehicle (unless some active cooling system is employed). The ablation process (sublimation and reactions involving solid char and pyrolysis of other resins composing the virgin material) divert a significant fraction of the convective and radiative energy flux away from the heat shield bond line. Examples of missions that require(d) some level of coupled radiation and ablation analyses include Apollo, Orion, Stardust, Pioneer Venus, and Galileo.

The numerical simulation of coupled radiation and ablation has progressed over the past 30 years from viscous shock layer methods<sup>1</sup> to upwind based finite-volume methods.<sup>2-4</sup> Implementation details for the present work on coupled radiation and ablation differ in some important ways. In recent papers describing coupled radiation and ablation, Matsuyama<sup>2</sup> simplifies the system by modeling only two effective species, gas from the free stream and ablation gas which are each characterized by constant elemental mass fraction. Fujita<sup>3,4</sup> includes a comprehensive thermochemical nonequilibrium flow model in conjunction with a species mass continuity boundary condition that includes reaction probabilities at the wall and a specified pyrolysis gas species mass fraction blowing rate. The present method assumes chemical equilibrium at the wall with the net elemental flux from blowing and diffusion balanced by the specified elemental mass fraction of the ablation products. An option is retained in which gas chemistry in the shock layer can be calculated at equilibrium by employing partial equilibrium relations to supplement elemental continuity or by full chemical nonequilibrium employing species continuity. In either case, the original species densities are retained as fundamental dependent variables.

This paper is a companion to the recent papers by Johnston et. al.<sup>5,6</sup> Whereas these companion papers focus on specific applications, the present paper focuses on the modeling and the numerical details of model implementation. The baseline flow solver is a newly refactored version of the LAURA code<sup>7</sup> that utilizes Fortran 95 modules. The physics modules described herein (as well as the refactored LAURA) are a subset of the FUN3D<sup>8</sup> suite of modules so that they are available to that unstructured flow solver.

### III. Free Energy Minimization - (FEM)

#### A. Overview

The Gibbs Free Energy minimization (FEM) option is implemented with a goal of making simple adjustments to the baseline thermochemical nonequilibrium flow solver to enable a thermochemical equilibrium solver for generic mixtures of gases with spatially varying elemental mass fractions. The capability is required to enable interfaces with ablation routines based on equilibrium gas chemistry. The capability also enables simulations that are so deep into the equilibrium regime that the magnitude of species chemical source terms overwhelm the magnitude of convection and diffusion. (Roundoff error in the evaluation of the source terms is significant relative to the magnitude of convective and diffusive terms.) Consequently, the sum of the species continuity equations does not telescope to a meaningful mixture continuity equation because of roundoff error. The modification is implemented as follows.

1. A parser is added to extract the constituent elements from the species names.
2. Basis species are identified as the simplest homogeneous particle (smallest molecular weight, usually the atom) corresponding to each constituent element.
3. Partial equilibrium relationships (derived from free energy minimization) for each remaining species are based on the following criteria.
  - (a) Neutral molecules are equilibrated to constituent base species
  - (b) Ionized heavy particles are equilibrated with electron and corresponding neutral base.
4. The species continuity equations corresponding to base species in the baseline thermochemical nonequilibrium solver are replaced with elemental conservation equations. The elemental conservation equations are formed from an appropriate linear combination of species conservation equations already present in the baseline algorithm. The electron continuity equation is replaced by an algebraic relation among species to force net charge neutrality.

5. The species continuity equations corresponding to non-base species in the baseline thermochemical nonequilibrium solver are replaced with algebraic, partial equilibrium relations from step 3.
6. The baseline solver (point-implicit or line-implicit relaxation) is applied to the modified system of equations. Even though elemental conservation equations are present the dependent variable set retains the use of the original set of species, never using elemental densities directly.

The algorithm described here has limitations. The algorithm fails if any element does not appear as a homogeneous component of one of the species. The algorithm does not handle solid carbon in the mix of species although an equilibrium state with solid carbon at the surface can be utilized to compute sublimation temperature. The partial equilibrium relations potentially can be very stiff (large magnitude of transformed equilibrium constant  $K_j$  defined below) because no consideration is given to local conditions that may govern a better selection of equilibrating species. In fact, a floor on equilibrium constant is applied which kicks in at temperatures less than 1000 K. The impact of this floor is that the mass fractions of trace species may be in error at low temperatures but the consequence of the error is in the noise. The algorithm could be modified to address any of these limitations but in tests conducted to date the simple approach described here is sufficient.

## B. Elemental Continuity Equations

The transformation from species continuity to elemental continuity involves the identification of the fraction of element  $i$  in each species  $j$ . The transformation matrix  $\mathbf{F}$  involves  $N_e$  rows, one for each element, and  $N_s$  columns, one for each species. The fraction is computed by multiplying the elemental weight,  $\tilde{M}_i$  by the number of atoms of that element in the species,  $\tilde{\alpha}_{i,j}$  and dividing by the species weight  $M_j$ .

$$F_{i,j} = \frac{\tilde{\alpha}_{i,j}\tilde{M}_i}{M_j} \quad (1)$$

Consider the one-dimensional species conservation equations set.

$$\frac{\partial \mathbf{q}}{\partial t} + \frac{\partial \mathbf{f}}{\partial x} = \dot{\mathbf{w}} \quad (2)$$

where  $\mathbf{f}$  includes convection and diffusion. If one multiplies both sides of Eq. 2 by  $\mathbf{F}$  one obtains the elemental conservation equations

$$\mathbf{F} \left[ \frac{\partial \mathbf{q}}{\partial t} + \frac{\partial \mathbf{f}}{\partial x} \right] = \mathbf{F} \dot{\mathbf{w}} \quad (3)$$

$$\frac{\partial \tilde{\mathbf{q}}}{\partial t} + \frac{\partial \tilde{\mathbf{f}}}{\partial x} = \mathbf{0} \quad (4)$$

Note that  $\mathbf{F}\dot{\mathbf{w}} \equiv \mathbf{0}$ . Chemical reactions cannot create or destroy an element in the control volume. Still, it is important to apply the transformation matrix before adding the source term because the critical components of continuity through convection and diffusion may be of the order of roundoff error in the assembly of the source term  $\dot{\mathbf{w}}$ . The assembly of the Jacobian of the elemental conservation laws (Eq. 12) employs the same matrix transform and retains the use of species densities (rather than elemental densities) as the fundamental dependent variables. Consequently, the remaining non-base species must be replaced by a partial equilibrium relation in order to close the equation set for species densities.

## C. Partial Equilibrium Relations

The derivation of partial equilibrium relations through the minimization of free energy is available in several texts.<sup>9</sup> Consider the partial equilibrium relation for non-base species  $j$  which may be expressed as

$$\sum_m^{reactants} \beta_{m,j} M_m \rightleftharpoons \sum_n^{products} \beta_{n,j} N_n \quad (5)$$

where one of the products  $N_n$  corresponds to non-base species  $j$ , the reactants correspond to constituent base species, and one additional species may be required to enforce a chemical balance. The partial equilibrium relation involving non-base species  $j$  may then be derived as follows.

$$\Delta F_j^0 = -RT \ln \left[ \frac{\prod_{n=products} \bar{p}_n^{\beta_{n,j}}}{\prod_{m=reactants} \bar{p}_m^{\beta_{m,j}}} \right] \quad (6)$$

$$\frac{\Delta F_j^0}{RT} + \sum_n \beta_{n,j} \ln \frac{\bar{R}T}{M_n} - \sum_m \beta_{m,j} \ln \frac{\bar{R}T}{M_m} = - \sum_n \beta_{n,j} \ln \rho_n + \sum_m \beta_{m,j} \ln \rho_m \quad (7)$$

$$\sum_n \beta_{n,j} \left( \frac{H_n - TS_n}{RT} + \ln \frac{\bar{R}T}{M_n} \right) - \sum_m \beta_{m,j} \left( \frac{H_m - TS_m}{RT} + \ln \frac{\bar{R}T}{M_m} \right) = - \sum_n \beta_{n,j} \ln \rho_n + \sum_m \beta_{m,j} \ln \rho_m \quad (8)$$

$$K_j(T) = \sum_k^{species} G_{j,k} \ln \rho_k \quad (9)$$

where  $\bar{R} = \rho_\infty R / 101325$ . to include conversion from pressure in atmospheres to the metric system and to non-dimensionalize density by  $\rho_\infty$ . The non-base species continuity equations are thus replaced by a linear equation in  $\ln \rho_k$  with coefficients defined

$$G_{j,k} = \begin{cases} 0 & \text{if species } k \text{ is not part of reaction } j \\ -\beta_{n,j} & \text{if species } k = n \text{ is a product in reaction } j \\ \beta_{m,j} & \text{if species } k = m \text{ is a reactant in reaction } j \end{cases} \quad (10)$$

The temperature dependent equilibrium constant  $K_j(T)$  is curve fit using

$$K_j(T) = A_j \frac{1}{Z} + B_j + C_j \ln Z + D_j Z + E_j Z^2 \quad (11)$$

where  $Z = 10000./T$  and the constants  $A_j - E_j$  are defined by fitting to the left-hand-side of Eq. 8 at  $T = 1000., 2000., 4000., 8000., 16000$ . The enthalpy  $H_n$  and entropy  $S_n$  for species  $n$  is obtained from curve fits.<sup>10</sup>

The coupled solution of Eq. 9 with the other conservation laws can be a challenge, particularly when it is early in the simulation and the solution is far from a converged state. It has been found that ignoring the Jacobian of Eq. 9 with respect to temperature and by multiplying the Jacobian of Eq. 9 with respect to species densities by a safety factor of 15 has enabled solution of the FEM coupled equation set for all tests conducted for this paper. The factor 15 was determined through numerical experiment.

## IV. Ablation Boundary Conditions

The ablation boundary condition derived here assumes there will be coupling with an ablation module such as FIAT<sup>11</sup> in conjunction with an equilibrium chemistry module. It is assumed that ablation mass flow rate  $\dot{m} = \dot{m}_{pyrolysis} + \dot{m}_{char}$ , the elemental composition of ablation gases  $\tilde{c}_{i,abl}$ , and the temperature of the ablating surface are supplied by the ablation module or can be user specified. The ablation module itself requires the aerothermodynamic environments (pressure, radiative and convective heating, and possibly shear) over time to compute material response. Consequently, a boundary condition must be applied to the flow solver that closes the equation sets for either nonequilibrium external flow using species continuity equations or equilibrium external flow using elemental continuity equations. As noted in the previous section the species densities are retained as the fundamental dependent variable data set regardless of the assumption of equilibrium state of the external flow.

It is assumed that gas chemistry at and within the ablating heatshield is in an equilibrium state. A steady, one-dimensional, elemental continuity equation (Eq. 12) describes the flow of an equilibrium gas across the boundary that accounts for convection and diffusion of element  $i$ .

$$\frac{\partial \tilde{\rho}_i v}{\partial y} = \frac{\partial \tilde{\rho}_i \tilde{V}_i}{\partial y} \quad (12)$$

Because we wish to work directly with species densities the transformation matrix introduced in the previous section is applied in Eq. 13 below.

$$F_{i,j} \frac{\partial \rho_j v}{\partial y} = F_{i,j} \frac{\partial \rho_j V_j}{\partial y} \quad (13)$$

where summation over species  $j$  is implied.

Integrate Eq. 13 over  $y$  from some virtual point sufficiently deep in the heatshield where it is assumed that the net elemental mass flux is given by  $\tilde{c}_{i,abl}\dot{m}$ . This assumption ignores the possibility that ablating mass flux sources are distributed through the depth of the char. Short of simulating flow through the char it is not clear that this modeling assumption can be improved. The resulting relation (Eq. 14) provides a balance for each element in which the convected elemental mass flux out of the boundary minus the diffused elemental mass flux into the boundary must equal the ablated elemental mass flux specified for the material.

$$F_{i,j}\rho_j v - \tilde{c}_{i,abl}\dot{m} = F_{i,j}\rho_j V_j \quad (14)$$

$$F_{i,j}\rho_j v - \tilde{c}_{i,abl}\dot{m} = F_{i,j}\rho D_j \frac{\partial \chi_j}{\partial y} \quad (15)$$

Note that an effective binary diffusion coefficient is applied to model diffusive flux. A mass corrected diffusive flux<sup>12</sup> is also applied to guarantee that the sum of diffusive flux over all species (or over all elements) goes to zero. Simulations show some elemental separation near the wall for the no blowing case. Elemental separation in the no-blowing case is less when modeling multi-component diffusion using the Stefan Maxwell equations.<sup>12</sup> A verification check shows that no elemental separation is computed in the no-blowing case when a constant Schmidt number is applied.

The discretization of Eq. 15 is shown in Eq. 16. It is necessary to solve for all dependent variables in the ghost cell 0.

$$F_{i,j} \left[ \frac{(\rho_j v)_1 + (\rho_j v)_0}{2} \right] - \tilde{c}_{i,abl}\dot{m} = F_{i,j} \left[ \frac{(\rho D_j)_1 + (\rho D_j)_0}{2} \right] \left[ \frac{\chi_{j,1} - \chi_{j,0}}{\Delta y} \right] \quad (16)$$

The solution in the ghost cell requires simultaneous relaxation of the partial equilibrium relations given by Eq. 9. The Jacobian formed using  $\ln \rho_j$  as the dependent variable provides a more robust convergence of this boundary condition. A relaxation factor is applied to each row of the Jacobian according to the magnitude of the current residual for that row equal to  $n/(d \ln[\rho_j]^2 + n)$  where  $n$  is the local iteration count on relaxation steps for this boundary condition. Note that in the limit of zero blowing this boundary condition specifies an equilibrium catalytic wall - that is, the species are in chemical equilibrium as determined by the wall temperature and pressure and elemental mass fraction gradient equal to zero.

$$\frac{1}{2} [(\rho v)_1 + (\rho v)_0] = \dot{m} \quad (17)$$

$$p_1 + \rho_1 v_1^2 = p_0 + \rho_0 v_0^2 \quad (18)$$

The equation set is closed with a discretization of net mass flux (Eq. 17) and normal momentum balance (Eq. 18). Eq. 17 is used to eliminate  $v_0$  from all equations. Then Eq. 18 replaces one of the elemental continuity equations so that the ghost cell pressure  $p_0$  is consistent with the specified temperature  $T_0 = 2T_w - T_1$  and the computed densities  $\rho_{j,0}$ .

At present, ablation rates and ablation gas elemental mass fractions are explicitly set by the user. The boundary condition is sufficiently robust to enable a coupled simulation assuming equilibrium gas chemistry at  $V_\infty = 15$  km/s and a dimensionless blowing rate equal to 0.2.

On the first step of initialization, all cells (including ghost cells) are set to inflow conditions. On the second step of initialization ghost cell velocities are reset to zero and wall temperatures are set to a user specified value. Simulations involving ablation and/or radiation are started from a converged (or nearly converged) non-radiating and non-ablating solution. The line-implicit formulation for relaxation of interior cells requires a Jacobian of the boundary condition. It is assumed for this purpose that species mass fractions and temperature in the ghost cells are fixed. (The point-implicit formulation for relaxation of interior points, by definition, requires no Jacobian information of neighbor cells.)

During interior cell updates the surface convective heating, shear, and diffusion flux are calculated from current values in the ghost cells. Ghost cell values in turn are updated at a user defined frequency,  $N_{exchange}$ . (Ghost cells are also used to hold information from neighbor blocks and the variable name  $N_{exchange}$  derives from the frequency in which neighbor block information is exchanged.) Ghost cell values of species density are fully defined by interior point values - there is no time dependent update or damping using any fraction of a previous value. Damping is applied to the update of a radiative equilibrium surface temperature in the case of no blowing. The radiative equilibrium wall temperature boundary condition is then defined with  $T_w^{new} = \varepsilon[q/(\epsilon\sigma)]^{1/4} + (1 - \varepsilon)T_w^{old}$ . In this case, the ghost cell temperature is computed as  $T_0 = 2T_w - T_1$ .

$N_{exchange}$  is set equal to 2 in all cases presented herein. The temperature damping factor  $\varepsilon$  is varied between 0.001 and 0.01. In more recent applications (some involving a surface energy balance not covered here) the combination  $N_{exchange} = 20$  and  $\varepsilon = 0.1$  have provided more robust convergence.

## V. Radiation Coupling

Radiative energy transport is computed using the tangent slab approximation with the HARA code.<sup>13,14</sup> The flow solver provides species densities, temperatures, and distances along a ray orthogonal to the surface as inputs to HARA. HARA returns divergence of the radiative flux and radiative flux to the wall for use in LAURA. Calls are made to HARA on the order of hundreds of relaxation steps,  $N_{rad}$ , holding the radiative quantities constant over this period (loosely coupled). Options are provided to interpolate radiative quantities between selected rays to reduce overall time in the radiation solver. The HARA radiation model treats atomic lines and continuum of N, O, C, and H. Molecular bands are treated for N<sub>2</sub>, N<sub>2</sub><sup>+</sup>, O<sub>2</sub>, NO, C<sub>2</sub>, C<sub>3</sub>, CN, CO, C<sub>2</sub>H. Non-Boltzmann electronic state models are applied for atoms and molecules. Typical computational time for a single line-of-sight is 20 to 50 seconds - short enough to enable fully coupled simulations with codes like LAURA.

A parameter  $f_{rad}$  may be specified to introduce the divergence of the radiative flux more slowly into the flow solver.

$$\nabla \cdot \mathbf{q}_{rad}^{n+1} = f_{rad} \nabla \cdot \mathbf{q}_{rad}(\text{HARA}) + (1 - f_{rad}) \nabla \cdot \mathbf{q}_{rad}^n \quad (19)$$

If the radiation introduces strong cooling into the shock layer the shock standoff distance decreases significantly. As the captured shock moves closer to the body, computational cells previously in the hot shock layer are overtaken by the pre-shock domain. However, these cells retain the cooling term  $\nabla \cdot \mathbf{q}_{rad,i,j,k}$  from the previous call to the radiation solver. The LAURA code enforces a floor on temperature for every point in the flowfield that allows the simulation to survive such transients under most circumstances. However, cases have been observed where introduction of the full update to radiation has caused stability problems. Best practice so far has been to set  $f_{rad}$  to 0.4 on the first call from an uncoupled solution and then to increase its value to 1 on subsequent returns from the radiation solver.

## VI. Results and Discussion

Three test cases are presented to demonstrate that the algorithms for coupled multiphysics (radiation plus ablation plus flow solver) indeed work and that they provide credible simulations (consistent with existing flight data and benchmark simulations). All cases were run on an Intel based Mac laptop, each simulation requiring on the order of two to four hours for 10000 to 20000 relaxation steps. Courant numbers varied from 5 to 50 (local time stepping). (More recent work suggests that constant time stepping with time steps equal to time for free stream to travel 0.001 m is more efficient.) Further details of each case are provided in the original sources.

### A. Fire II, Coupled Radiation Only

The Fire II data set from 1967 remains the touchstone for validation of entry heating simulations of radiative heating.<sup>15-17</sup> The vehicle had three overlaid beryllium heatshields. A fresh surface was exposed twice during entry after the outermost heatshield was jettisoned as its integrity became compromised due to thermal load. Consequently, radiation data was obtained without the complications of ablation products. Metallic surfaces are generally considered to be strongly catalytic but the potential formation of an oxide coating introduces uncertainty in the proper formulation of this boundary condition. Therefore results are presented using

bounding approximations for a super-catalytic condition (species mass fractions on the surface equal to free stream values) and for a non-catalytic condition (zero species fraction gradient at the wall). Surface temperatures were specified according to flight data.

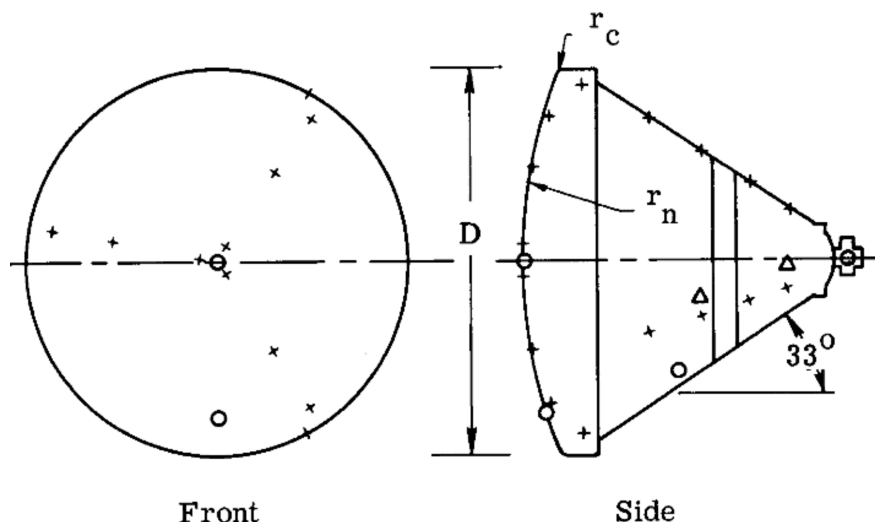


Figure 1. Sensors on Fire II vehicle, circle represents radiometer locations, x represents calorimeter locations.

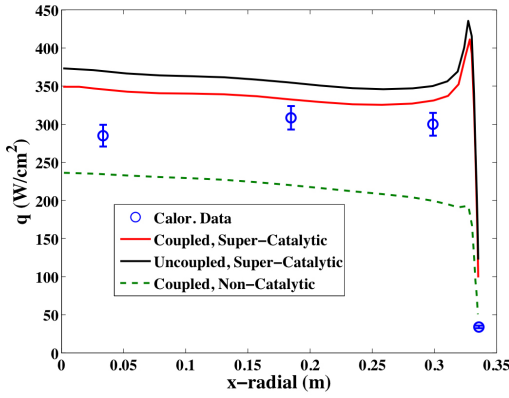
Instrument locations are presented in Fig. 1. The radiometers record radiation intensity contribution between 0.4 and 6.2 eV (window limits). The calorimeters record total convective and absorbed radiative heating. The absorbed radiative energy is calculated as a function of wavelength.<sup>18</sup> Simulations at two trajectory points are intended to illustrate capabilities at a strong thermochemical nonequilibrium condition (1636 seconds) and a near-equilibrium condition (1643 seconds).

The computed heating rates for the subject points are compared to experimental data in Fig. 2. The total heating rates measured by the calorimeters are presented in Figs. 2 (a) and (b). The solid black line in these figures indicate the uncoupled total heating (radiative heating computed from converged, non-radiating case) assuming a super-catalytic boundary condition. The solid red line indicates the total heating with full coupling of radiative energy transfer. The coupling reduces the total heating by 5 to 10 % for these trajectory points. The dashed lines indicate the coupled, non-catalytic heating rate. The catalytic effect is most prominent (reduction by 1/3) at the strong nonequilibrium point at 1636 seconds. The catalytic effect is still evident at 1643 seconds with a net reduction of 5 %. The experimental data, indicated by blue circles, is fully bounded by the extremes in modeling of surface catalysis. The uncoupled radiation intensity is presented with a dashed line and the coupled radiation intensity is presented with a solid red line in Figs. 2 (c) and (d). The uncertainty in the experimental data in these figures (blue circles and error bar) bounds the computed coupled results. The simulations indicate that radiation coupling is required to match experimental data and that the suite of physical models used to compute these cases are consistent with experimental data.

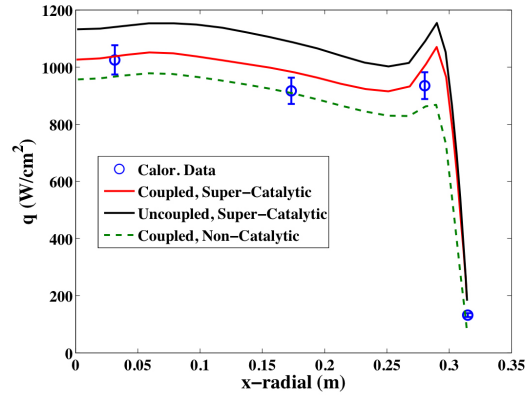
## B. Mars Return, Coupled Radiation and Ablation, Equilibrium Shock Layer

The Mars return example has been extensively studied for over 30 years, beginning with the then state-of-the-art viscous shock layer (VSL) code methodology.<sup>1,19,20</sup> The cases are useful because shock layer profiles and parametric studies are available for comparison in the literature. The VSL simulations used a fitted shock boundary and equilibrium chemistry. The LAURA simulations are the first to work this case with a shock capturing algorithm. This case also demonstrates the Free Energy Minimization routine with elemental continuity equations replacing the species continuity equations. Free stream conditions for flow over a 3.05 m radius sphere are  $V_\infty = 15.24$  km/s,  $\rho_\infty = 0.000255$  kg/m<sup>3</sup>. Elemental mass fractions of injected gas are  $[C, H, O, N] = (0.92, 0.022, 0.049, 0.009)$ . The wall temperature is set to 3600 K and the dimensionless

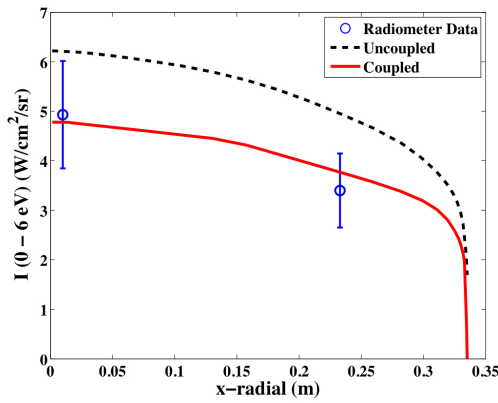




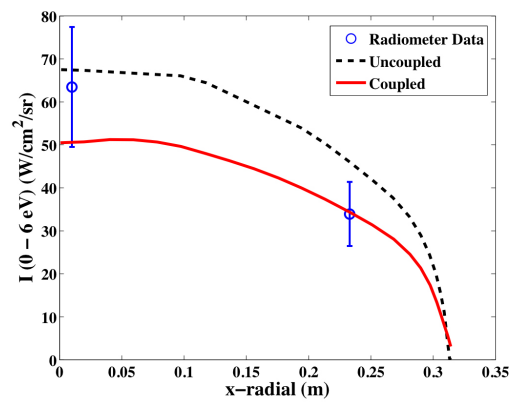
(a) Total heating distribution at 1636 seconds.



(b) Total heating distribution at 1643 seconds.



(c) Radiation intensity distribution at 1636 seconds.



(d) Radiation intensity distribution at 1643 seconds.

**Figure 2.** Total and radiative heating distributions around Fire II vehicle at trajectory points 1636 and 1643.

blowing rate  $\dot{m}$  is set to 0. (no ablation) and 0.2.

Stagnation streamline profiles of temperature and wall directed radiative flux computed by LAURA / HARA (solid lines) and VSL<sup>1</sup> (dashed lines) are compared in Fig. 3. Three cases are compared: (1) non-ablating, non-radiating; (2) non-ablating, coupled radiating; and (3) coupled ablating, coupled radiating. The non-radiating profile shows a constant temperature across the inviscid portion of the shock layer, as expected for an equilibrium gas. The shock layer cooling with radiation and associated decrease in shock standoff distance is evident in the middle set of curves of Fig. 3 (a). Note that the dashed lines from Moss in this figure end abruptly at the fitted shock used in the VSL algorithm. The ablating case shows a large increase in the boundary layer thickness ( $\approx 3$  cm) and corresponding displacement of the bow shock. The wall directed radiative flux in Fig. 3 (b) indicates absorption of photon flux in the ablation products near the wall. In all cases the LAURA / HARA simulations are in good agreement with the earlier VSL results - demonstrating consistency with a previous formulation of this coupled physics simulation. More details of this case, including comparisons with other methods, are available in the literature.<sup>5</sup>

### C. Apollo 4, Coupled Radiation and Ablation

The Apollo 4 test case, recently reviewed by Park,<sup>21</sup> provides flight data on radiative heating including effects of ablation products. Free stream conditions are  $V_\infty = 10.25$  km/s and  $\rho_\infty = 0.000341$  kg/m<sup>3</sup> on a 3. meter radius sphere. Elemental mass fractions of injected gas are  $[C, H, O, N] = (0.63, 0.06, 0.30, 0.01)$ . These fractions were derived from data discussed by Park<sup>21</sup> in which quasi-steady ablation is assumed and the elemental fractions of char and pyrolysis gas are combined according to the fraction of their individual

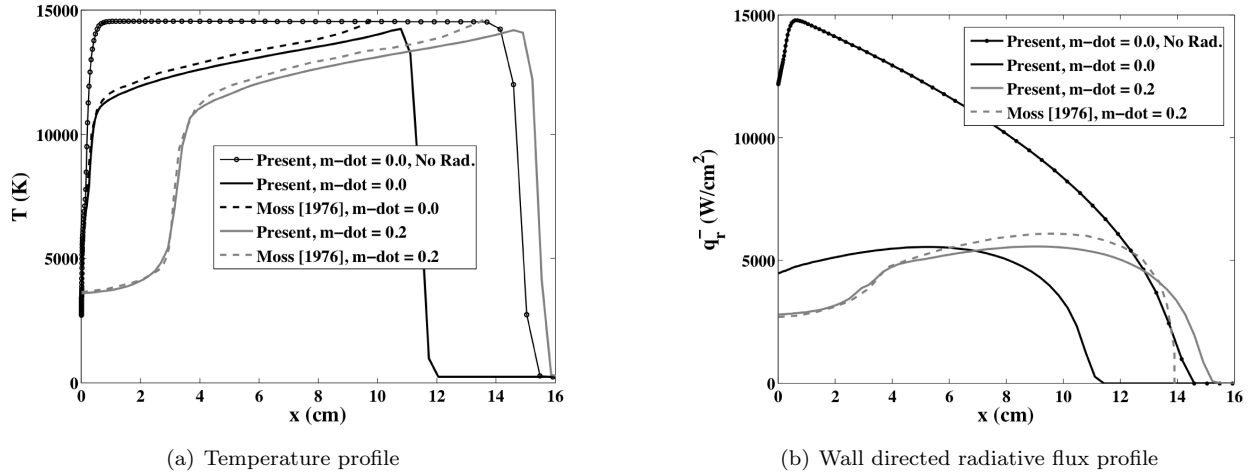


Figure 3. Stagnation streamline profiles for Mars return benchmark case.

blowing rates. The wall temperature is set to 2500 K and the dimensionless blowing rate  $\dot{m}$  is 0.0086.<sup>21</sup> Thermochemical nonequilibrium model is applied. The case was initialized from a non-ablating solution in which the equilibrium catalytic wall boundary condition was applied.

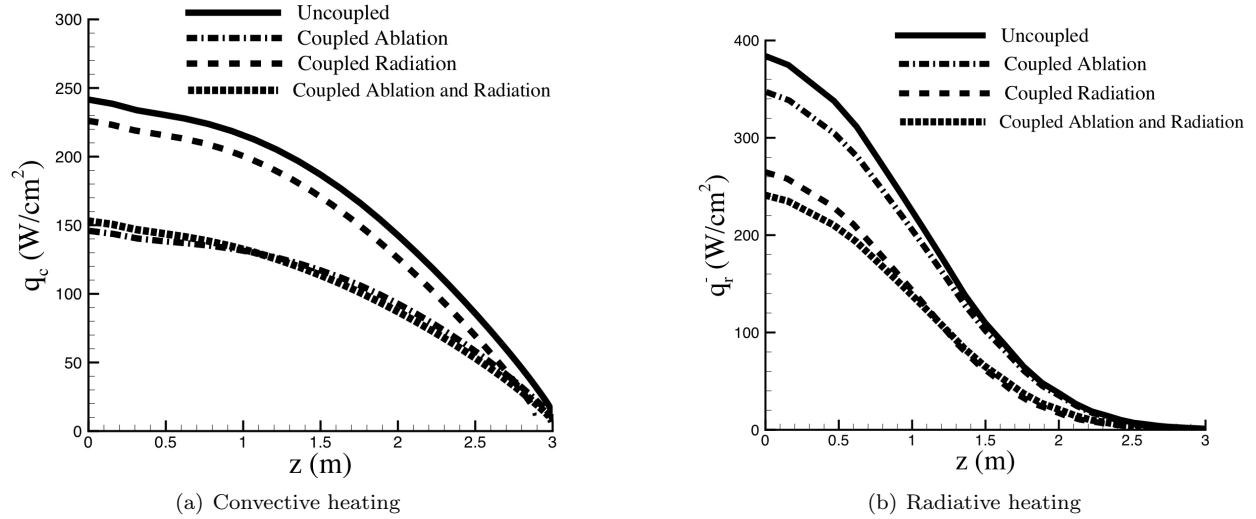
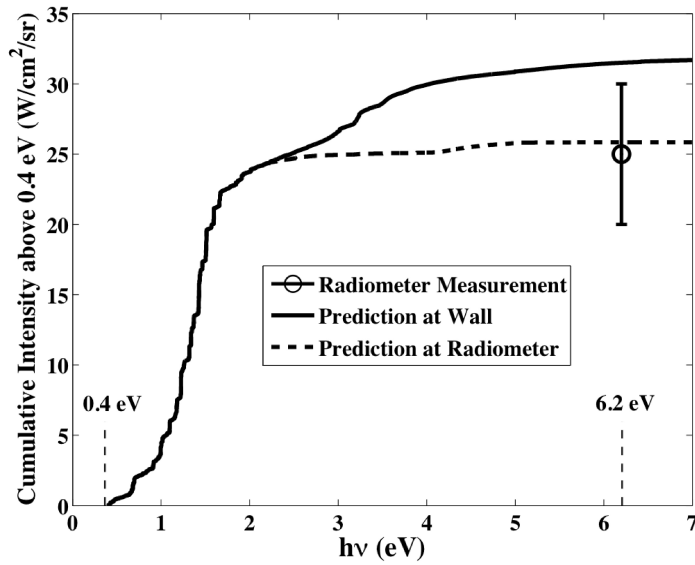
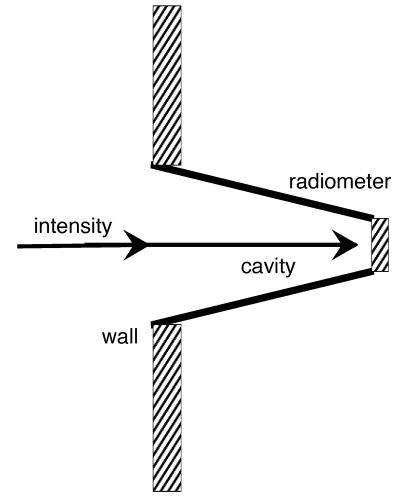


Figure 4. Surface heating distributions for Apollo 4 entry with and without radiation and ablation coupling.

Fig. 5 (a) plots the cumulative intensity arriving at the radiometer starting from 0.4 eV and concluding at 6.2 eV (the radiometer window is opaque outside this range). The path length indicated by the solid line includes the shock-layer thickness immediately above the radiometer. The path length indicated by the dashed line includes the shock-layer thickness plus 8 cm of cavity depth (Fig. 5 (b)) which is assumed to be filled with gas at conditions on the surface. (There was no flow field simulation that included a cavity.) From 0.4 to approximately 2.0 eV there is essentially no difference in the intensity reaching the radiometer over either path length. The intensity reaching the radiometer above 2eV becomes path length dependent, indicating that some of the radiation above 2eV is being absorbed by the gas in the cavity. The circular symbol with uncertainty bar indicates the measured cumulative intensity. It is convenient to put this symbol at the end of the window range at 6.2 eV but the data in fact represents the integrated intensity from 0.4 to 6.2eV. This figure shows that for the assumed blowing conditions the predicted cumulative intensity at the surface exceeds the measure value by approximately 20 %. However, if the effect of absorption over a longer



(a) Intensity integrated over frequency over two paths



(b) Extra path length through cavity to radiometer

Figure 5. Comparisons with Apollo 4 radiometer data.

path length through the cavity is included then excellent agreement with measurement is obtained.

We caution that this agreement does not constitute validation. The specified blowing rates and elemental mass fraction of the ablation products are estimates<sup>21</sup> - not computed on any first principles within this simulation. Still, the results confirm that for a reasonable estimate of boundary conditions there is consistency with measured data - providing more supporting evidence that the coupled radiation and ablation algorithms are correctly implemented. Further details of this simulation with more consideration of parametric variation is available in the literature.<sup>5</sup>

## VII. Concluding Remarks

A description of models and boundary conditions required for coupling radiation and ablation physics to a hypersonic flow simulation finite-volume solver is provided. The focus herein is to present the algorithmic details (relaxation factors, update frequency, approximations to the Jacobians) that are required to maintain a stable, fully coupled simulation. Three application examples are then provided (FIRE II, Mars return, and Apollo 4 applications) to illustrate that: (1) - the new modules are correctly implemented; and, (2) - the results are consistent with either experimental data or prior, benchmark calculations.

Chemical equilibrium routines for varying elemental mass fraction are required in the flow solver to integrate with the equilibrium chemistry assumption employed in the ablation models. This capability is provided through a strong coupling of partial equilibrium relations derived through Free Energy Minimization (FEM). The FEM capability also enables an equilibrium catalytic wall boundary condition in the non-ablating case.

The HARA code, using a tangent slab approximation, forms the basis of the radiation solver. Its relatively quick solution time per line of sight (20-50 seconds) makes the fully coupled solution process tenable. The ablation is currently modeled using a user specified mass flow rate and user specified elemental mass fractions of the blown gas. Work is ongoing to compute a char ablation rate based on equilibrium of gaseous carbon at the wall with solid carbon in the char and to couple this system with the FIAT<sup>11</sup> code to compute the pyrolysis gas rates.

The FIRE II test cases include the entire forebody surface distributions and compare them to experimental heating data. The predicted heating rates for super-catalytic and non-catalytic boundary conditions bound the experimental data. The predictions for radiative intensity are within the uncertainty bounds of the

measured data. The Mars return test cases demonstrate the application of FEM over the entire shock layer including ablation products. Ablation coupling has the strongest impact on convective heating and milder impact on radiative heating in this case - indicative of the effect of absorption by ablation gases. Radiation coupling has the strongest impact on radiative heating and milder impact on convective heating. Computed results are consistent with benchmark solutions obtained with a Viscous Shock Layer (VSL) approach. The Apollo 4 test case shows good agreement with a cumulative radiation intensity measurement through a shock layer including absorption through a boundary layer with ablation gases. These comparisons are collected here in one place to demonstrate code capability and consistency with available data for a challenging array of problems.

Future work will engage an equilibrium state between atomic carbon and char along with a surface energy balance to compute a char blowing rate. Then coupling with FIAT will be introduced to handle the physics of pyrolysis gas without filtering through a blowing correction. A capability to automatically run a sequence of trajectory points from a user supplied file is currently running. It is planned to capture the heating history for input to FIAT. Finally, a quasi-one-dimensional grid adaptation capability will be modified to enable shape change as a function of the distributed blowing rates and the trajectory history.

## References

- <sup>1</sup>Moss, J. N., "Radiative Viscous-Shock-Layer Solutions with Coupled Ablation Injection," *AIAA J.*, Vol. 14, No. 9, Sept. 1976, pp. 1311-1317.
- <sup>2</sup>Matsuyama, S., Ohnishi, N., Sasoh, A., and Sawada, K., "Numerical Simulation of Galileo Probe Entry Flowfield with Radiation and Ablation," *J. Therm. and Heat Trans.*, Vol. 19, No. 1, Jan. 2005, pp. 28-35.
- <sup>3</sup>Fujita, K., Yamada, T., and Ishii, N., "Impacts of Ablation Gas Kinetics on Hyperbolic Entry Radiative Heating," AIAA Paper 2006-1185, Jan. 2006.
- <sup>4</sup>Fujita, K., Matsukawa, Y., Yamada, T., and Ishii, N., "Evaluation of heat Transfer Rates of Venus Entry Capsules Along Flight Trajectories," AIAA Paper 2006-3580, Jun. 2006.
- <sup>5</sup>Johnston, C. O., Gnoffo, P. A., and Sutton, K., "The Influence of Ablation on Radiative Heating for Earth Entry," AIAA Paper 2008-4107, Jun. 2008.
- <sup>6</sup>Johnston, C. O., Gnoffo, P. A., and Thompson, R. A., "Coupled Ablation Analysis for Orion Heatshields," AIAA Paper 2009-0674, Jan. 2009.
- <sup>7</sup>Cheatwood, F. M. and Gnoffo, P. A., "User's Manual for the Langley Aerothermodynamic Upwind Relaxation Algorithm (LAURA)," NASA TM 4674, April 1996.
- <sup>8</sup>Anderson, W. K. and Bonhaus, D. L., "An Implicit Upwind Algorithm for Computing Turbulent Flows on Unstructured Grids," *Comp. and Fluids*, Vol. 23, No. 1, Jan. 1994, pp. 1-21.
- <sup>9</sup>Glassman, I., *Combustion*, Academic Press, 1977.
- <sup>10</sup>McBride, B. J., Zehe, M. J., and Gordon, S., "NASA Glenn Coefficients for Calculating Thermodynamic Properties of Individual Species," NASA TP 2002-211556, September 2002.
- <sup>11</sup>Chen, Y.-K. and Milos, F. S., "Ablation and Thermal Response Program for Spacecraft Heatshield Analysis," AIAA Paper 98-0273, January 1998.
- <sup>12</sup>Sutton, K. and Gnoffo, P. A., "Multi-component Diffusion with Application to Computational Aerothermodynamics," AIAA Paper 98-2575, Jun. 1998.
- <sup>13</sup>Johnston, C. O., "A Comparison of EAST Shock-Tube Radiation Measurements with a New Air Radiation Model," AIAA Paper 2008-1245, Jan. 2008.
- <sup>14</sup>Johnston, C. O., "Nonequilibrium Shock-Layer Radiative Heating for Earth and Titan Entry," Virginia Tech dissertation, Nov. 2006.
- <sup>15</sup>John H. Lewis, J. and Scallion, W. I., "Flight Parameters and Vehicle Performance for Project FIRE Flight II, Launched May 22, 1965," Tn, NASA, August 1966.
- <sup>16</sup>Cauchon, D. L., "Radiative Heating results from the FIRE II Flight Experiment at a Rentry Velocity of 11.4 Kilometers per Second," Tm, NASA, July 1967.
- <sup>17</sup>Cauchon, D. L., McKee, C. W., and Cornette, E. S., "Spectral measurements of Gas-Cap Radiation During Project FIRE Flight Experiment at Rentry Velocities near 11.4 Kilometers per Second," Tm, NASA, Oct 1967.
- <sup>18</sup>Johnston, C. O., Hollis, B. R., and Sutton, K., "Nonequilibrium Stagnation-Line Radiation for FIRE II," *J. Spacecraft and Rockets*, Vol. 45, No. 6, Nov-Dec 2008.
- <sup>19</sup>Garrett, L. B., Smith, G. L., and Perkins, J. N., "An Implicit Finite-Difference Solution to the Viscous Shock Layer, Including the Effects of Radiation and Strong Blowing," Nasa tr, 1972.
- <sup>20</sup>Gupta, R. N., Lee, K. P., Moss, J. N., and Sutton, K., "Viscous Shock Layer Solutions with Coupled Radiation and Ablation Injection for Earth Entry," *J. Spacecraft and Rockets*, Vol. 29, No. 2, 1992, pp. 173-181.
- <sup>21</sup>Park, C., "Stagnation-Point Radiation for Apollo 4," *J. Therm. and Heat Trans.*, Vol. 18, No. 3, July 2004, pp. 349-357.